Supporting Information

Rationalizing the promotional effect of Mn oxides in benzene combustion using O 2p-band center descriptor

Lipeng Wang, Zhiwei Huang*, Yueyao Du, Sufeng Guo, Guohua Jing.

Department of Environmental Science & Engineering, College of Chemical Engineering, Huaqiao University, Xiamen, Fujian 361021, China

***Corresponding authors: zwhuang@hqu.edu.cn (Z. Huang)**

Experimental Section

Materials and reagents: $FeCl_3 \cdot 6H_2O$ (99%), $Ce(NO_3)_3 \cdot 6H_2O$ (99.95%), $Mn(NO_3)_2 \cdot 4H_2O$ (98%), $Co(NO_3)_2 \cdot 6H_2O$ (98.5%), $Cu(NO_3)_2 \cdot 3H_2O$ (99%), CH_3COONa, and anhydrous alcohol (99.7%). All the reagents were used as received without further purification or modification.

Catalyst preparation: Hexagonal Fe_2O_3 plate (α-Fe_2O_3) was synthesized by hydrothermal reaction method. Firstly, 10 mM $FeCl_3 \cdot 6H_2O$ was dissolved in a mixture of 60 mL of ethanol and 4.2 mL of deionized water to a concentration of 10 mmol L^{-1}. 4.80 g of CH_3COONa was then added in this mixture under continuously stirring. The mixture was transferred Teflon-lined autoclave and kept at 180 ^oC for 12 h in an oven. The red slurry obtained was filtered and washed several times with deionized and absolute ethanol. The final composite was dried at 80 ^oC, and then calcined at 400 ^oC for 2 h. MO_x/Fe_2O_3 was prepared by impregnation of MO_x from their nitrate or chloride salts onto hexagonal Fe_2O_3 plate support. Typically, 1.0 g of α-Fe_2O_3 flake was suspended in 10 mL of deionized water under magnetic stirring. $Ce(NO_3)_3 \cdot 6H_2O$, $Co(NO_3)_2 \cdot 6H_2O$, $Cu(NO_3)_2 \cdot 3H_2O$, or $FeCl_3 \cdot 6H_2O$ was then added to this mixture to a metal concentration of 23 mmol L^{-1}. The mixture was heated to 80 ^oC until dried. The final product was dried at 80 ^oC for 12 h, and then calcined at 400 ^oC for 2 h.

Material characterization: Crystallographic information of catalysts was obtained with X-ray diffraction (XRD, Rigaku Corporation SmartLab X-ray diffractometer). Morphology and structure were measured using transmission electron microscope (TEM, FEI Tecnai G2 F30 transmission electron microscope). H_2 temperature programmed reduction (H_2-TPR) was carried out on Micromeritics Autochem 2920 equipped with a thermal conductivity detector (TCD). X-ray photoemission spectroscopy (XPS) experiments were carried out using a Thermo Scientific Escalab 250Xi. The binding energies of all elements were corrected by the standard C1s line at 284.6 eV. The metal content analyses of the samples were performed via inductively coupled plasma optical emission spectroscopy (ICP-OES) (Agilent 5110 instrument).

Performance evaluations: The reaction was carried out with a quartz tube fixed bed microreactor. Catalysts were tableted, granulated, and sieved (40-60 mesh) prior to use. For benzene combustion measurements, 0.1 g of catalysts was loaded into the reactor. Feed gas containing 10 vol% O_2, 500 ppm benzene, balanced with N_2 was allowed to pass through the reactor at a flow rate of 100 mL min^{-1}, and the gas hour space velocity (GHSV) was estimated to be GHSV = 60,000 mL g^{-1} h^{-1}. The catalytic activity was calculated based on the following equation:

$$Benzene\ Conversion = \left(1 - \frac{C_{Benzene(in)}}{C_{Benzene(out)}}\right) \times 100\%$$

Where $C_{Benzene(in)}$ and $C_{Benzene(out)}$ represent the concentrations of benzene inlet and outlet, respectively. The concentration of benzene was measured by a Fuli GC-9790 II gas chromatograph equipped with flame ionization detectors (FID) and a TCD.

Additional Discussion

X-ray diffraction: We characterized the crystal phases of MO_x/Fe_2O_3 catalysts and Fe_2O_3 by X-ray diffraction (XRD). As shown in Figure S1a, the powder XRD pattern for Fe_2O_3 shows reflections consistent with phase-pure rhombohedral hexagonal Fe_2O_3 [power diffraction file (PDF) no. 33-0664]. The 2 theta angels of peaks in the pattern from the CuO_x/Fe_2O_3 are in line with the standard pattern for pure Fe_2O_3 phase [S1], demonstrating that the structure of the Fe_2O_3 support had been preserved. There exists an overlap between the peaks of CuO(-111), CuO(002) and that of Fe_2O_3(110). According to the coming high-resolution transmission electron microscopy (HRTEM) images (Figure S2), the supported CuO nanoparticles have a rounded shape, distinctly different from the geometry of Fe_2O_3 support. The lattice of the supported particle (Figure S2) matches well with the crystal structure of monoclinic CuO phase (PDF no. 45-0937). Therefore, the CuO_x/Fe_2O_3 is denoted as CuO/Fe_2O_3 hereafter. For CoO_x/Fe_2O_3, XRD patterns of the sample displayed discernable peak that could be indexed as that of Co_3O_4(311) with a cubic symmetry (space group Fm-3m, PDF no. 43-1003). The CoO_x/Fe_2O_3 is designated as Co_3O_4/Fe_2O_3 hereafter. For Fe_2O_3 supported CeO_x, an additional set of relatively weak peaks in the XRD pattern, corresponding to CeO_2(111) and CeO_2(220), is observed. These weak diffractions derive from the cubic CeO_2 phase (space group Fm-3m, PDF no. 34-0394). Hence, the CeO_x/Fe_2O_3 is named as CeO_2/Fe_2O_3 hereafter. The XRD pattern for FeO_x/Fe_2O_3 shows reflections consistent with phase-pure Fe_2O_3. For MnO_x/Fe_2O_3, only the hkl reflections of Fe_2O_3 support were sufficiently sharp for indexing in XRD pattern, confirming that the MnO_x was in a highly dispersed form. Figure S1b shows the powder diffraction patterns for x wt% MnO_x/Fe_2O_3 (x = 2-64) catalysts. Two additional peaks appeared in the spectrum of high-loading sample of 64 wt% MnO_x/Fe_2O_3, which were assigned to tetragonal MnO_2 phase (space group P42/mnm, PDF no. 24-0735). The MnO_x/Fe_2O_3 catalysts synthesizing at low MnO_x loadings are likely to have the same MnO_2 structure, as extrapolating from the XRD analysis of 64 wt% MnO_x/Fe_2O_3. Therefore, the MnO_x/Fe_2O_3 sample shown in Figure S1b is hereafter labelled as MnO_2/Fe_2O_3. The crystal phases obtained from XRD studies for MO_x/Fe_2O_3 catalysts are summarized in Table S1.

Transmission electron microscope: Figure S2 reveals the morphologies of MO_x/Fe_2O_3 and the pristine Fe_2O_3. The pristine Fe_2O_3 support had a hexagon-like shape (Figure S2a). MO_x loading has no effect on the morphology of the Fe_2O_3 support. As shown in Figure S2b-f, the morphology of Fe_2O_3 support in MO_x/Fe_2O_3 catalysts largely maintained the hexagonal shape. Conversely, the MO_x oxides attached directly to the Fe_2O_3 surface and accommodated a spherical geometry, which minimized their surface energy.

X-ray photoemission spectroscopy: Crystal phases of supported MO_x were collaborated by measurements of the valence states with XPS. XPS spectrum for Mn 2p indicates the presence of Mn^{4+} as the major species (Figure S3a), which is consistent with our XRD analyses. The binding energy matches well with the literature values. In the case of supported Co_3O_4, which is mixture valence states of Co^{2+} and Co^{3+}, we saw satellite features due to the Co^{2+} state (Figure S3b). The Ce 3d core-level spectrum of CeO_2/Fe_2O_3 is presented in Figure S3c. The Ce 3d spectrum from Ce^{4+} has six visible peaks, even though there is only one valence state [S2]. XPS peaks with labels of *v* and *u* correspond to the Ce $3d_{3/2}$ and Ce $3d_{5/2}$ core levels, while other labels, including *v*, *v''*, *u* and *u''* represent satellite features arising from the Ce $3d_{3/2}$ and Ce $3d_{5/2}$ ionization. The XPS data reveal that the Ce^{4+} is the

dominating species in CeO_2/Fe_2O_3, consistent with XRD results (Figure S1). For CuO/Fe_2O_3, significant Cu^{2+} satellite features are seen in the Cu 2p core-level spectrum of Figure S3d [S3], confirming the predominant presence of CuO. For all MO_x/Fe_2O_3, strong satellite features of Fe^{3+} at 724 eV are observed [S4]. And there is almost no shift in Fe $2p_{3/2}$ peaks. Therefore, the XPS measurements reveal no charge transfer between the active phases and the Fe_2O_3 support. This finding suggests that no strong interactions exist between MO_x and Fe_2O_3 in MO_x/Fe_2O_3. The electronic effects of the surface oxygen species have also been considered (Figure S3f). The O 1s spectra of MO_x/Fe_2O_3 catalysts exhibited two spectral features: the main component at low binding energy (529.3 eV) is assigned to surface lattice oxygen (O_β), and the component at 531.0 eV to low-coordinated or adsorbed O^- ions (O_α) present on surface of the catalysts. These two features can be qualitatively deconvoluted by means of a least-squares fit of multiple Gaussian peaks. Catalysts containing high O_α/O_β ratio are predicted to be catalytically more active compared to catalysts with a low O_α/O_β, as suggested by previous reports [S5]. Figure S4 and Table S1 show O_α/O_β ratios of MO_x/Fe_2O_3. However, the data for O_α/O_β ratio of the MO_x/Fe_2O_3 do not correlate with the observed activity trend as shown in Figure 3.

Surface area, bulk composition, and surface metal content: Surface area was one of the structural descriptors; Brunauer-Emmett-Teller (BET) measurements show that the MO_x/Fe_2O_3 catalysts present similar surface areas, with surface areas of 23 ± 3 m^2 g^{-1} in all the samples (Table S1). The small variations in the surface area data indicate that the descriptor of surface area cannot explain the differences in the performance. The bulk composition of M/Fe (atom%) and MO_x (wt%) were obtained with the aid of ICP-OES (Table S1). Therefore, we excluded this parameter from discussions of the performance change. The surface metal contents of MO_x/Fe_2O_3 catalysts were characterized using XPS. As shown in Table S1, no significant correlations were observed between the surface metal contents and the measured catalytic activities. The above results show that the structural parameters, including the surface area, bulk composition, and surface metal content, are not the descriptors dominating the catalytic activity and the type of transition metal oxide.

Electronic descriptors: Such quantitative information. Electrons in a material can be exited from the valence band to the conduction band. Electron transition occurs when the materials absorb a phonon (heat-induced transition) or a photon (light-induced transition). Width of the forbidden band between valence band and conduction band is known as band gap. Center of O 2p-band is defined as the centroid of the O 2p density states. The d-band center is the center of the d-type density states relative to the Fermi level [S6]. The band gap, top of the valence band, bottom of the conduction band, center of O 2p-band, and d-band center data for MO_x were obtained from sophisticated theoretical calculations in previous works [17-21], and are shown in Table S2.

Table S1. Physical properties and benzene combustion rates of MO_x/Fe_2O_3 materials.

Sample	Surface metal content of M[a] [atom %]	Bulk composition[b]		Crystal phases[c]	Surface area [$m^2\ g^{-1}$]	O_α/O_β	Reaction rate (300 °C) [mol benzene $g^{-1}\ s^{-1}$]
		M/Fe [atom %]	MO_x [wt %]				
MnO_2/Fe_2O_3	23	8.35	8.33	MnO_2	20.4	0.29	6.88×10^{-7}
CuO/Fe_2O_3	11	8.54	7.84	CuO	21.9	0.55	6.25×10^{-8}
FeO_x/Fe_2O_3	100	-	-	Fe_2O_3	22.0	0.39	5.06×10^{-9}
Co_3O_4/Fe_2O_3	25	7.28	5.51	Co_3O_4	20.5	0.63	1.47×10^{-7}
CeO_2/Fe_2O_3	17	5.53	10.64	CeO_2	25.9	0.34	4.90×10^{-8}

[a] Surface metal content was determined by XPS.

[b] Bulk composition was calculated by ICP-OES.

[c] From XRD and XPS measurements

Table S2. Potential electronic descriptors of MO_x (M = Cu, Fe, Mn, Co, Ce).

Transition metal oxide	Top of valence band [eV]	Bottom of conduction band [eV]	d-band center [eV]	Center of O 2p band [eV]	Band gap [eV]	Reference
CuO	-0.98	2.46	-6.73	-4.24	3.44	[17]
Fe_2O_3	0	1.90	-2.75	-2.25	1.90	[18]
MnO_2	0	0.27	-4.32	-3.53	0.27	[19]
Co_3O_4	0	2.23	-2.57	-2.73	2.23	[20]
CeO_2	0	2.5	-2.57	-1.44	2.50	[21]

Table S3. Benzene combustion activity over transition metal oxides in the previous literature.

Catalysts	Reaction Conditions [a]	Benzene Conversions	Reference
8 wt% MnO_2/Fe_2O_3	10 vol% O_2, 500 ppm benzene WHSV = 60,000 mL g^{-1} h^{-1}	T_{90} = 270 °C	This work
$8.5CrO_x/\gamma\text{-}Al_2O_3$	30 vol% O_2, 1000 ppm benzene WHSV = 20,000 mL g^{-1} h^{-1}	T_{90} = 340 °C	[S7]
$MnO_2/Ce_{0.75}Zr_{0.25}O_2$	21 vol% O_2, 2000 ppm benzene WHSV = 72,000 mL g^{-1} h^{-1}	T_{90} = 340 °C	[S8]
12.5% $V_2O_5/\gamma\text{-}Al_2O_3$	21 vol% O_2, 1000 ppm benzene WHSV = 12,000 mL g^{-1} h^{-1}	T_{90} = 322 °C	[S9]
7% $CuO/Ce_{0.7}Mn_{0.3}O_2$	21 vol% O_2, 1000 ppm benzene WHSV = 12,000 mL g^{-1} h^{-1}	T_{90} = 265 °C	[S10]
$Co_3O_4/\alpha\text{-}Fe_2O_3$	20 vol% O_2, 290 ppm Benzene WHSV = 85,700 mL g^{-1} h^{-1}	T_{90} = 375 °C	[S11]
15% MnO_x/TiO_2	20 vol% O_2, 500 ppm benzene WHSV = 60,000 mL g^{-1} h^{-1}	T_{90} = 310 °C	[S12]
$LaCoO_3$/SBA-15	21 vol% O_2, 500 ppm benzene WHSV = 96,000 mL g^{-1} h^{-1}	T_{90} = 330 °C	[S13]
11 wt% $Cu_xMn_yO_z/SiO_2$	21 vol% O_2, 580 ppm benzene WHSV = 20,000 mL g^{-1} h^{-1}	T_{90} =275 °C	[S14]
CoCe(18:1)/SBA-16	21 vol% O_2, 1000 ppm benzene GHSV = 80,000 h^{-1}	T_{90} =300 °C	[S15]

[a] GHSV and WHSV are short for “Gas Hour Space Velocity” and “Weight Hour Space Velocity”, respectively.

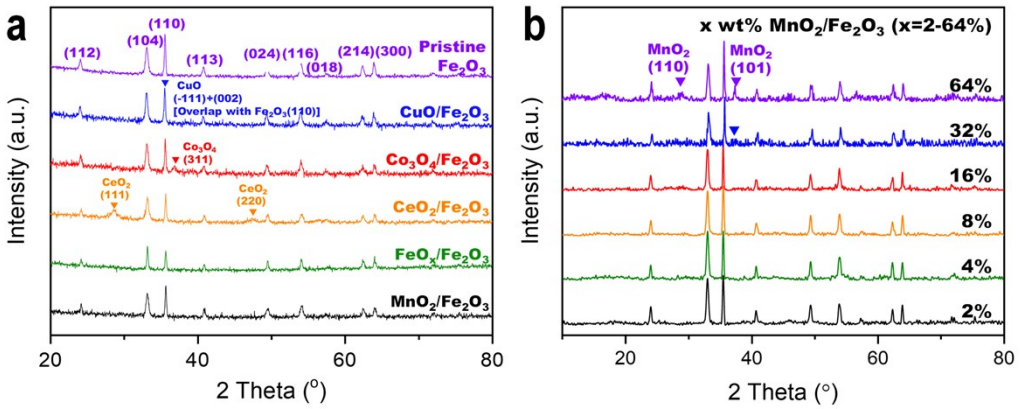

Figure S1. (a) XRD patterns of the MO_x/Fe_2O_3 and pristine Fe_2O_3 support. (b) XRD patterns for x wt% MnO_x/Fe_2O_3 (x=2-64) catalysts

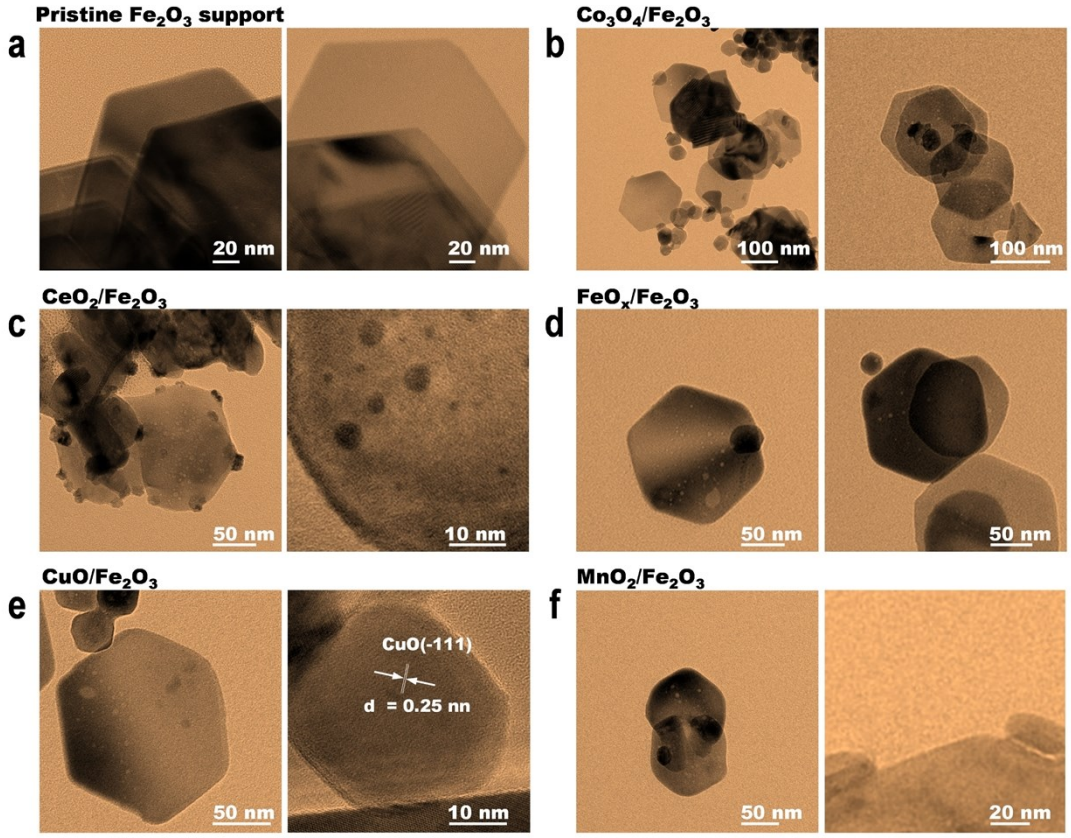

Figure S2. TEM images of catalysts: (a) pristine Fe_2O_3, and (b-f) MO_x/Fe_2O_3 (M= Co, Ce, Fe, Cu or Mn.)

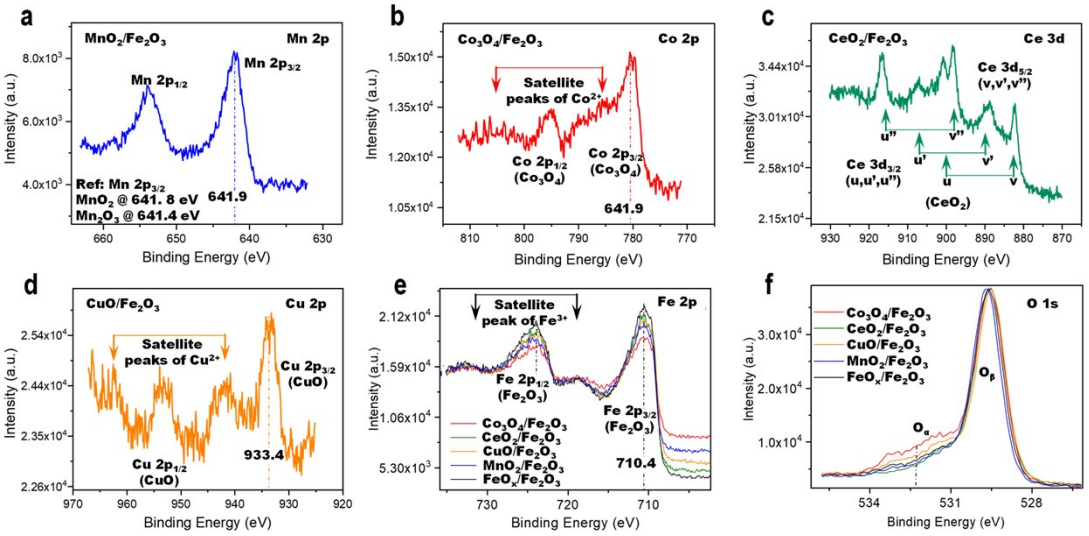

Figure S3. XPS spectra of MO_x/Fe_2O_3 catalysts, (a) Mn 2p, (b) Co 2p, (c) Ce 3d, (d) Cu 2p, (e) Fe 2p and (f) O 1s level.

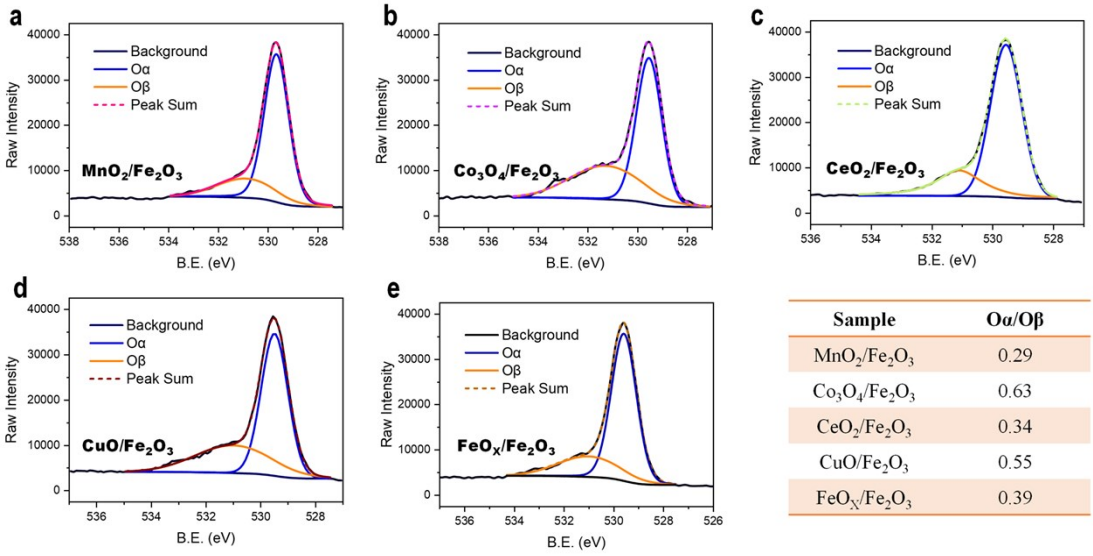

Sample	Oα/Oβ
MnO_2/Fe_2O_3	0.29
Co_3O_4/Fe_2O_3	0.63
CeO_2/Fe_2O_3	0.34
CuO/Fe_2O_3	0.55
FeO_X/Fe_2O_3	0.39

Figure S4. O 1s spectra and O_α/O_β ratios of MO_x/Fe_2O_3 samples.

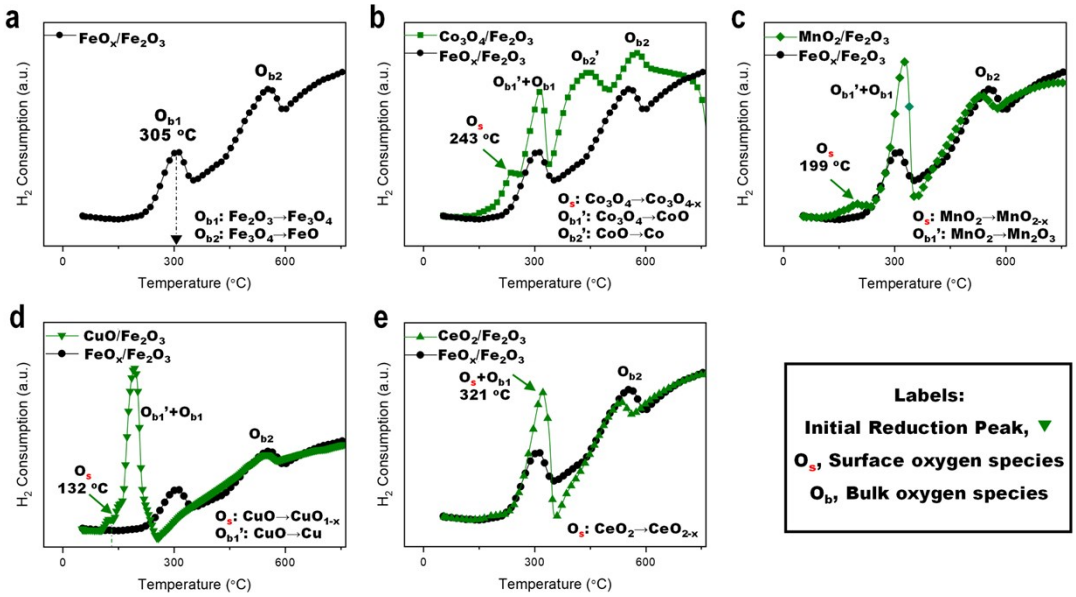

Figure S5. H_2-TPR profiles of: (a) FeO_x/Fe_2O_3, (b) Co_3O_4/Fe_2O_3, (c) MnO_2/Fe_2O_3, (d) CuO/Fe_2O_3, and (e) CeO_2/Fe_2O_3. The profile of FeO_x/Fe_2O_3 was used for comparison in (b-e) to aid peak identification.

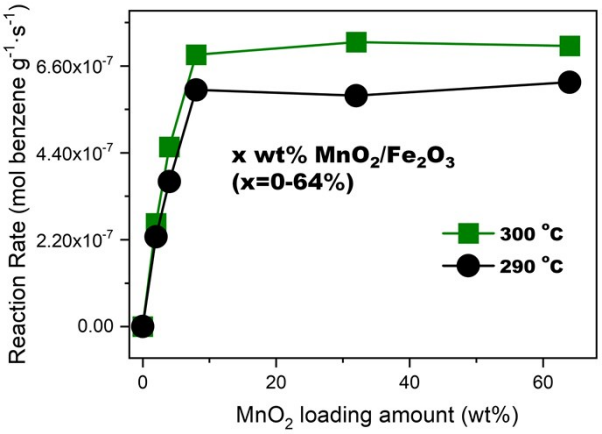

Figure S6. Benzene combustion rates of MnO_x/Fe_2O_3 as a function of MnO_x loading at 290 and 300 °C.

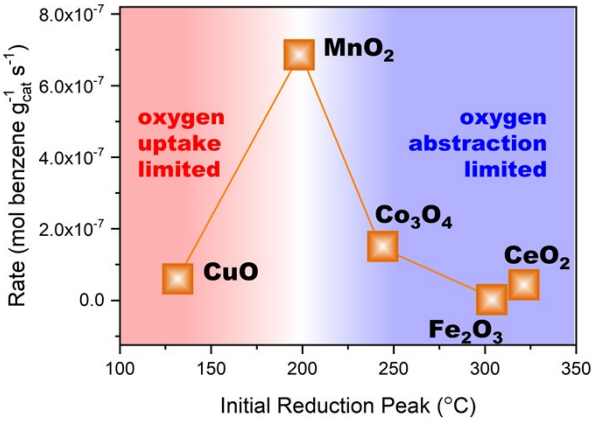

Figure S7. The scaling relation of the O 2p-band center of TMOs with their initial reduction peak.

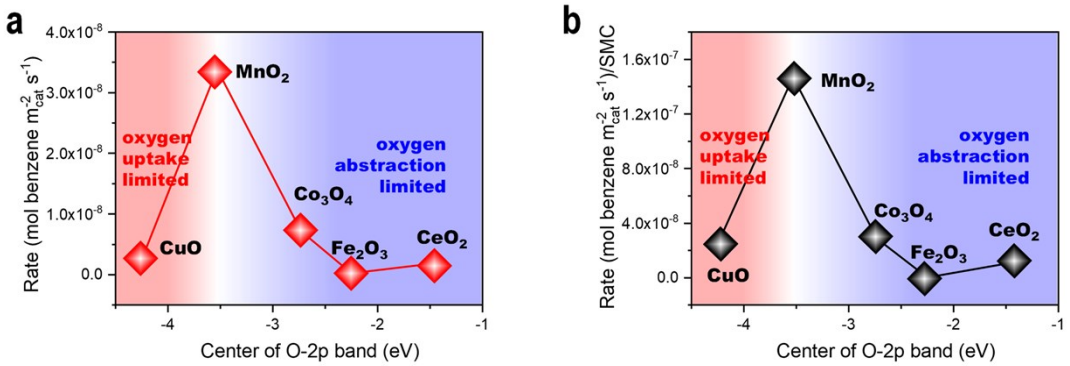

Figure S8. The scaling relation of the O 2p-band center of MOx with surface-area-normalized (a) or surface-area-surface-composition-jointly-normalized (b) benzene catalytic combustion rate. The SMC in (b) is short for "surface metal contents".

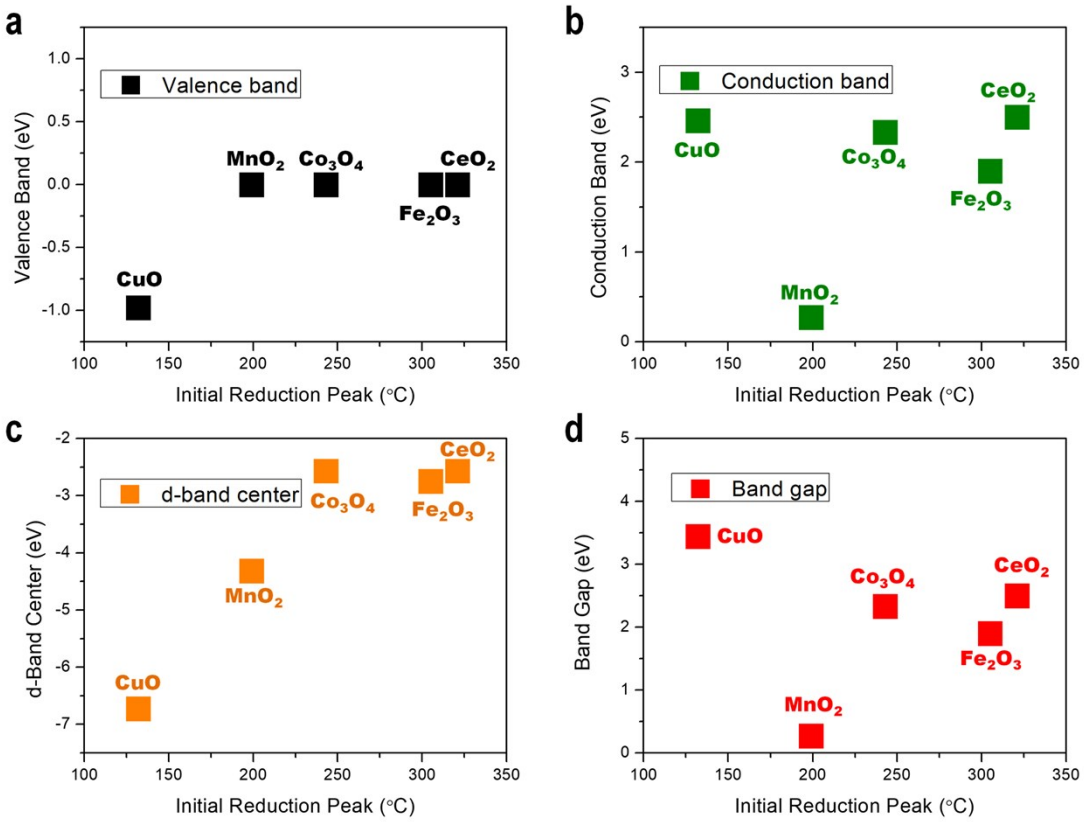

Figure S9. Illustration of scaling relations. The plots in (a-d) show how different electronic descriptors of band structures scale with the initial reduction peaks for MO_x/Fe_2O_3 samples.

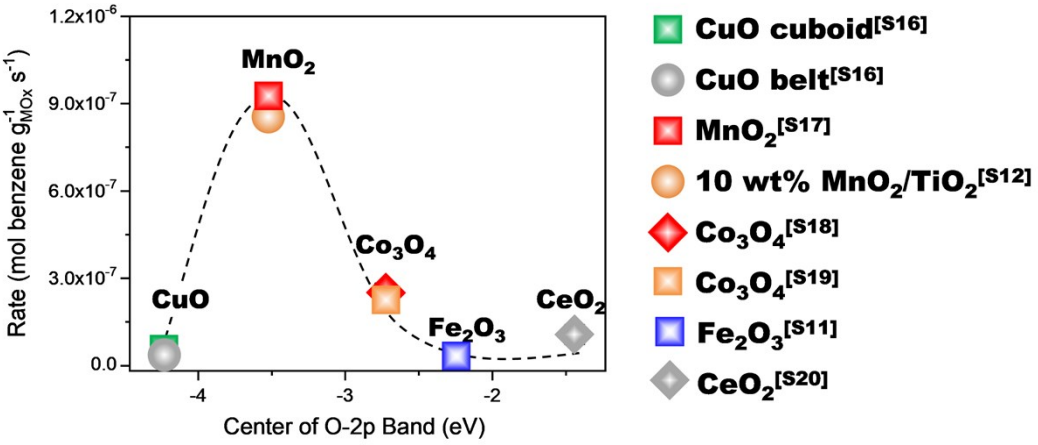

Figure S10. The scaling relation between benzene conversion rate (at 250 °C) of MO_x from literature with O 2p-band center.

References

S1. Z. Huang, Y. Du, J. Zhang, X. Wu, H. Shen, Y. Qian and G. Jing, *Catalysis Science & Technology*, 2018, **8**, 4702-4708.

S2. E. Bêche, P. Charvin, D. Perarnau, S. Abanades and G. Flamant, *Surface and Interface Analysis*, 2008, **40**, 264-267.

S3. L. Huang, F. Peng and F. S. Ohuchi, *Surface Science*, 2009, **603**, 2825-2834.

S4. R. Bliem, E. McDermott, P. Ferstl, M. Setvin, O. Gamba, J. Pavelec, M. A. Schneider, M. Schmid, U. Diebold, P. Blaha, L. Hammer and G. S. Parkinson, *Science*, 2014, **346**, 1215.

S5. T. E. Jones, T. C. R. Rocha, A. Knop-Gericke, C. Stampfl, R. Schlögl and S. Piccinin, *ACS Catalysis*, 2015, **5**, 5846-5850.

S6. J. K. Nørskov, F. Abild-Pedersen, F. Studt and T. Bligaard, *Proceedings of the National Academy of Sciences*, 2011, **108**, 937-943.

S7. T. Xing, H. Wan, Y. Shao, Y. Han, Z. Xu and S. Zheng, *Applied Catalysis A: General*, 2013, **468**, 269-275.

S8. I. C. Sophiana, A. Topandi, F. Iskandar, H. Devianto, N. Nishiyama and Y. W. Budhi, *Materials Today Chemistry*, 2020, **17**, 100305.

S9. P. Yang, J. Li, Z. Cheng and S. Zuo, *Applied Catalysis A: General*, 2017, **542**, 38-46.

S10. T.-Y. Li, S.-J. Chiang, B.-J. Liaw and Y.-Z. Chen, *Applied Catalysis B: Environmental*, 2011, **103**, 143-148.

S11. Y. Xiang, Y. Zhu, J. Lu, C. Zhu, M. Zhu, Q. Xie and T. Chen, *Solid State Sciences*, 2019, **93**, 79-86.

S12. J. L. Zeng, X. L. Liu, J. Wan, H. L. Lv and T. Y. Zhu, *J Mol Catal a-Chem*, 2015, **408**, 221-227.

S13. Y. Luo, K. Wang, J. Zuo, Q. Qian, Y. Xu, X. Liu, H. Xue and Q. Chen, *Molecular Catalysis*, 2017, **436**, 259-266.

S14. R. Fang, Z. Yang, X. Liu, Y. Yan, J. Ran and L. Zhang, *Fuel*, 2021, **286**, 119311.

S15. S. Zuo, F. Liu, J. Tong and C. Qi, *Applied Catalysis A: General*, 2013, **467**, 1-6.

S16. Z. Fei, P. Lu, X. Feng, B. Sun and W. Ji, *Catalysis Science & Technology*, 2012, **2**, 1705-1710.

S17. Z. Hu, R. Mi, X. Yong, S. Liu, D. Li, Y. Li and T. Zhang, *ChemistrySelect*, 2019, **4**, 473-480.

S18. Y. Liu, H. Dai, J. Deng, S. Xie, H. Yang, W. Tan, W. Han, Y. Jiang and G. Guo, *Journal of Catalysis*, 2014, **309**, 408-418.

S19. Q. Li, T. Odoom-Wubah, Y. Zhou, R. Mulka, Y. Zheng, J. Huang, D. Sun and Q. Li, *Industrial & Engineering Chemistry Research*, 2019, **58**, 2882-2890.

S20. S. M. Yang, D. M. Liu and S. Y. Liu, *Topics in Catalysis*, 2008, **47**, 101-108.